Material Profiling for Photocrystallography: Relating Single-Crystal Photophysical and Structural Properties of Luminescent Bis-Cyclometalated Iridium-Based Complexes

Jacqueline M. Cole,*[,†,‡,§] Katharine F. Bowes,[‡] Ian P. Clark,[⊥] Kian Sing Low,[†] Anita Zeidler,[‡,#] Anthony W. Parker,[⊥] Inamur R. Laskar,[‖,⊗] and Teng-Ming Chen[‖]

[†]Cavendish Laboratory, University of Cambridge, J. J. Thomson Avenue, Cambridge, CB3 0HE, U.K.

[‡]Department of Chemistry, University of Cambridge, Lensfield Road, Cambridge, CB2 1EW, U.K.

[§]Department of Chemistry, University of New Brunswick, P.O. Box 4400, Fredericton, NB E3B 5A3, Canada

[⊥]Central Laser Facility, Research Complex at Harwell, STFC Rutherford Appleton Laboratory, Harwell, Oxford, Didcot, Oxfordshire, OX11 0QX, U.K.

[‖]Department of Applied Chemistry, National Chiao Tung University, Hsinchu, 30050 Taiwan

S *Supporting Information*

ABSTRACT: The photophysical properties of seven luminescent iridium complexes are characterized in their single-crystal form, and the photoactivity is related to their molecular structures. Specifically, solid-state optical emission spectra and associated lifetimes are determined from single crystals of iridium complexes containing three bidentate ligands: two variously substituted 2-phenylbenzothiazoles and either a 2,4-pentadione (acetylacetone) or 2-pyridinecarboxylic (picolinic) acid. All complexes studied exhibit emissive behavior in the solid-state which originates from $^3\pi-\pi^*$ and metal-to-ligand-charge-transfer (MLCT) electronic transitions; this is supported by density functional theory. Phosphorescence is observed in all cases with microsecond lifetimes, ranging from 0.30 to 2.4 μs at 298 K and 1.4−4.0 μs at 100 K. Structure−property relationships are established which are relevant to the potential solid-state application of this series of luminescent complexes as organic light emitting diodes (OLED) material components. In addition, these materials are assessed for their suitability to time-resolved pump−probe photocrystallography experiments, which will reveal their photoexcited state structure. Accordingly, the design process by which materials are selected and technical parameters are defined for a photocrystallography experiment is illustrated. This family of complexes presents a case study for this photocrystallography material profiling. Results show that the time-resolved photoexcited state structure, featuring the MLCT transition is, in principle at least, viable for two of these complexes.
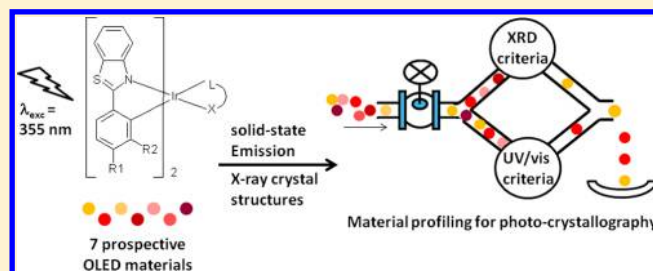
■ INTRODUCTION

Luminescent iridium-based complexes have generated much interest due to their beneficial photophysical and electrochemical properties.[1−4] In particular, they have prospective applications as phosphors in organic light emitting diodes (OLEDs) on account of their strong luminescence with high quantum efficiencies (solution-based quantum yields: 0.1−0.6) and microsecond excited state lifetimes.[5,6] OLEDs that contain heavy metal centers are inherently more efficient luminescent devices because of the spin-coupling associated with the metal. Iridium-containing OLEDs are among the most efficient.[7−9] Their luminescence properties arise from the lowest lying triplet state, thus overcoming the upper 0.25 efficiency limitation of organic fluorophores. Emission quantum yields are high in both solution phase and in the solid-state. The emission wavelength can be tuned by judicious selection of various ligands, which can be further refined by altering the ligand substituents.[10]

The cyclometalated nature of bis- and tris-chelate ligands offers particularly good emission wavelength tunability.[11] While bis-chelate iridium-based complexes are more common, tris-chelate complexes offer more opportunities for ligand design. This greater versatility is an important consideration when focusing on tuning the emission wavelength, as is a feature of this study.

The synthesis of tris-ligated cyclometalation to iridium is nontrivial, and so it is often easier to make iridium-based complexes that have two cyclometalated ligands and one spectator ligand, such as acetylacetone (acac), picolinic acid (pic), or *N*-methylsalicylimine-N,O (sal).[12] The seven complexes described in this paper have therefore been synthesized accordingly: each complex contains two cyclometalated
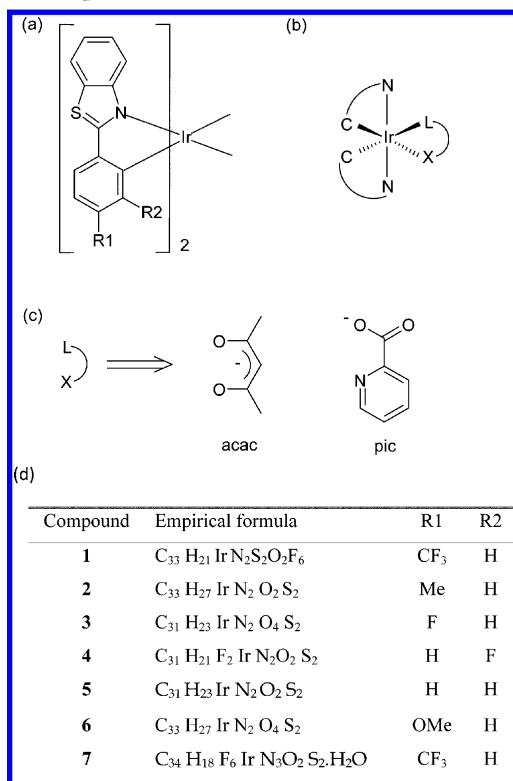
(bidentate) phenylbenzothiazole ligands and one bidentate monoanionic spectator ligand (acac or pic). A schematic diagram of the subject complexes is presented in Scheme 1.

Scheme 1. Schematic Structural Representations of the Subject Complexes[a]

Compound	Empirical formula	R1	R2
1	$C_{33} H_{21} Ir N_2 S_2 O_2 F_6$	CF_3	H
2	$C_{33} H_{27} Ir N_2 O_2 S_2$	Me	H
3	$C_{31} H_{23} Ir N_2 O_4 S_2$	F	H
4	$C_{31} H_{21} F_2 Ir N_2O_2 S_2$	H	F
5	$C_{31} H_{23} Ir N_2 O_2 S_2$	H	H
6	$C_{33} H_{27} Ir N_2 O_4 S_2$	OMe	H
7	$C_{34} H_{18} F_6 Ir N_3O_2 S_2.H_2O$	CF_3	H

[a]The 2-phenylbenzothiazole fragment (ĈN) has substituents in the *para-* (R1) or *meta-* (R2) positions, 4-CF$_3$ (**1**), 4-Me (**2**), 4-F (**3**), 3-F (**4**), 4-H (**5**), 4-OMe (**6**), and 4-CF$_3$ (**7**), as shown in (a), the coordination geometry of the complexes are shown in (b), and the identities of the LX ligands are shown in (c).

By varying the substituents on the phenylbenzothiazole ligands, it has been shown that one can fine-tune their solution-state photophysical properties.[13] The solid-state photophysical properties, however, have remained elusive. Yet, from a solid-state device application perspective, it is their solid-state photophysical properties which are most relevant. This paper seeks explicitly these photophysical properties in the solid-state together with their crystal structures, so that associated structure−property relationships unfold; acquiring such relationships stands to aid the fundamental 'molecular engineering' aspects that lie behind OLED device technology for iridium-based complexes.

While establishing these structure−property relationships represents a study in its own right, there is an additional motivation for this work. This concerns our desire to assess the suitability of these iridium-based complexes for a time-resolved (optical)pump-(X-ray) probe photocrystallography experiment, wherein the 4-D (space-time) photoexcited state crystal structure is determined.[14] This offers an exciting prospect since the comparison between ground and excited-state structure would provide a unique, direct, and quantitative insight into the function of iridium-complexes within OLED applications, at the molecular level.[15] Indeed, single-crystal X-ray diffraction is regarded as the 'gold standard' of structure determination. Contrast this with analogous time-resolved pump−probe UV/vis spectroscopy and related time-resolved vibrational spectroscopy which are more long-standing techniques, but which can only afford indirect and qualitative information about the nature of photoexcited states.

With that said, such 4-D 'photocrystallography' experiments present a very substantial experimental challenge.[16,17] They also require the use of a synchrotron source, access to which is rare and time-limited. So, wherever it is possible, all experimental parameters that are required for a photocrystallography experiment should be established well before the securing of synchrotron time.

The photophysical characteristics of a single-crystal sample represent one important set of such parameters. Indeed, the solid-state optical emissive properties and excited-state lifetime of the subject material dictate the very nature of the photocrystallography experimental setup.[14,17] A single crystal is used for these photocrystallography experiments, as changes in photophysical properties are very common between solid and solution state.

Another important set of experimental parameters to consider, prior to a photocrystallography experiment, is the nature of the ground-state crystal structure. The structural perturbations between ground and photoexcited state are usually very subtle. Any nonphoto-induced structural complication such as molecular disorder or libration therefore needs to be avoided, or else atomic resolution is compromised too heavily. The crystal-structure determination of this series of compounds, that forms part of this study, consequently serves to inform this assessment.

The concerted solid-state photophysical and structural characterization presented in this study therefore represents a very important prerequisite for assessing the suitability of a material for photocrystallography. Furthermore, solid-state versus solution-based optical spectroscopy measurements on the subject materials can be compared by reference to previous solution state experiments.[13]

In this paper, we show that for the iridium-based complexes studied here, the metal-to-ligand charge-transfer (MLCT) and intraligand (IL) state emissive characteristics are carried through to their single-crystal optical emission profiles. Their varying nature can be rationalized by arguments based on structure−property relationships that are associated with relative donor/acceptor strengths, chemical substitution patterns, and geometric distortions that affect charge-transfer. The IL state is found to be temperature dependent, with its emissive character disappearing at room temperature for some of the complexes. Microsecond-lived phosphorescence is observed which is indicative of ^{3}MLCT character. The structure−property relationships that unfold from this work are then employed to generate profiles of these complexes in terms of their prospects for a photocrystallography experiment. These material profiles are established via a generic, sequential decision-making process that best matches the idealized structure and photophysical properties for a photocrystallography experiment to those of each material in question. Additional considerations, which are specific to this particular family of complexes, show how one can narrow down the processed short-list to one target compound. In this case study, one iridium-based complex is ultimately chosen to go forward for characterization of its ephemeral photoexcited state structure.

■ EXPERIMENTAL AND COMPUTATIONAL METHODS

Syntheses. All the benzothiazole (bt) ligands and iridium(III) complexes, except for complex **7**, were synthesized using a literature method.[13] Complex **7** was synthesized by the following method. The chloride bridged dimer $(CF_3bt)_2Ir(\mu\text{-}Cl)_2(CF_3bt)_2$ (1 mmol) and picolinic acid (3 mmol) were taken in dichloromethane (30 mL) and refluxed for 12 h. After cooling, the volume of the reaction mixture was reduced by solvent removal. The residue was separated by filtration and the brown colored product recrystallized from a mixture of dichloromethane and methanol (yield 95%). ^{1}H NMR (300 MHz, CDCl₃): δ ppm 8.56 (d, 1H, 8.1 Hz), 8.24 (d, 1H, 7.8 Hz), 7.89 (m, 6H), 7.55 (m, 3H), 7.41 (t, 1H, 7.8 Hz), 7.22 (d, 2H, 7.8 Hz), 7.06 (t, 1H, 8.1 Hz), 7.03 (s, 1H), 6.43 (s, 1H), 6.15 (d, 1H, 5.7 Hz). FABMS: m/z 870, calc. 870.

Photophysical Measurements. The solution UV/vis absorption spectrum of **7** was collected on a Perkin-Elmer Lambda 20 spectrometer. Dilute solutions of the compounds, in dichloromethane, were placed in a quartz cuvette with path length of 1 mm. Analogous spectra for **1**–**6** were collected previously.[13]

Solid-state UV/vis emission and excitation spectra were collected at room temperature using a Jobin Yvon Horiba Fluoromax-3 spectrophotometer. The sample was in the form of a single-crystal, mounted onto a glass fiber.

Solid state (single-crystal) 100 K emission and lifetime data were obtained using a Monospec 600 monochromator and a photo-multiplier tube (PMT, EMI-GENCOM INC. RFI/QL-30F) with a 355 nm pump source (Continuum Powerlite 8000 Nd:YAG laser, c. 7 ns, 0.2 mJ/pulse) focused to c. 500 μm diameter spot. The sample was mounted on a metal pin and glass fiber, and emission was collected at 90° to the pump beam using an f/1 lens. The signal from the PMT was monitored using a Tektronix TDS3012 100 MHz oscilloscope triggered by a photodiode (EOT ET2000) picking up a small percentage of the pump light. Emission spectra were obtained by scanning through emission wavelengths and monitoring the change in intensity. Lifetime measurements were taken with the emission wavelength set at 625 nm and evaluated by modeling the intensity decay curves by a single exponential using the program Grace (Turner, 2003). Low temperatures were obtained using an open-flow nitrogen-based Oxford Cryosystems Cryostream cooling apparatus. A schematic illustration of the experimental setup is given in Figure 1.
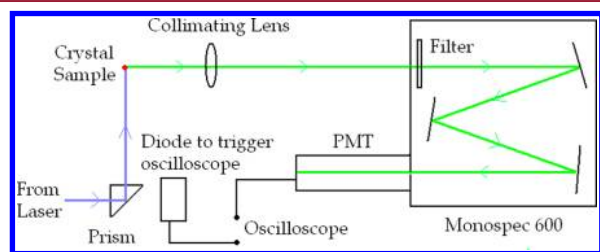
Figure 1. Schematic of the single-crystal UV/vis emission spectros-copy experimental setup.

X-ray Crystallography. Single crystal X-ray diffraction data were collected on compounds **1**–**7** at 180(2) K using a Nonius Kappa CCD diffractometer, equipped with graphite monochromated Mo–Kα (λ = 0.71073 Å) radiation, and employing an Oxford Cryosystems Cryostream nitrogen cooling device. Suitable single crystals were mounted onto glass fibers using perfluoropolyether oil. Cell parameters were refined against data from all regions of reciprocal space using HKLScalepack.[18] Data reduction employed HKLDenzo and Scalepack,[18] while the data sets were corrected for Lorentz and polarization effects and for absorption using SORTAV.[19] The structure was solved with direct methods within SHELXS-97, and refined by full-matrix least-squares methods on F² using SHELXL-97.[20] Position-al and anisotropic displacement parameters were refined for all non-hydrogen atoms, except for the disordered CF₃ groups in **7**, which

were modeled isotropically. Hydrogen atoms were placed in idealized positions relative to their adjoining carbon atom and refined within the constraints of a riding model. In the final cycles of refinement, a weighting scheme that gave a relatively flat analysis of variance was introduced and refinement continued until convergence was reached.

Details of data collection and refinement parameters are provided in Table 1. Full crystallographic information is provided in the Supporting Information.

Molecular disorder is present in the CF₃ groups of compounds **1** and **7**. This disorder was modeled as split sites in compound **7** (in a 50:50 occupancy ratio). Similarly, explicit modeling of disordered CF₃ groups in the crystal structure of **1** was attempted, but it compromised the accuracy of other more important bond parameters. As such, split sites were not included in the final model of **1**. The crystal structures of **1** and **2** have been reported previously at room temperature,[13,21] but the data collection here of **1** at 180 K enabled the nature of its molecular disorder to be classified as dynamic, as evident by the diminution of magnitudes of the anisotropic displacement parameters at 180 K compared with that at room temperature. It was also considered important to obtain both crystal structures **1** and **2** at the same temperature as the other structures reported in this paper such that comparisons between the structures of these complexes are temperature invariant.

Density Functional Theory (DFT) and Time-Dependent Density Functional Theory (TD-DFT). Quantum-chemical calcu-lations were performed on **1**–**7** using Gaussian 09.[22] Geometry optimizations employed the crystal structures presented herein as a starting point; where molecular disorder was manifest in the crystal structure, the predominant molecular component was used. For **4** and **7**, where $Z' = 2$ owing to concomitant molecular isomers, separate DFT and TD-DFT calculations were performed on each isomer. The resulting frontier molecular orbitals and oscillator strengths showed negligible difference between these isomers. Therefore, it was deemed acceptable to perform DFT and TD-DFT calculations on only one molecule in the asymmetric unit of **5** which presents a much more complicated case given $Z' = 8$. All molecular geometries were optimized with DFT using the Perdew, Burke and Ernzerhof (PBE0) functional[23−25] and a mixed basis set of LANL2DZ[26,27] for iridium and 6-31G(d) for all other atoms. A relativistic effective core potential (ECP) was also employed to model the iridium core electrons, leaving unconstrained just the outer layer $[(3s^2)(5p^6)]$ electrons and the $(5d^6)$ valence electrons. The PBE0 functional was chosen on the basis that it has been shown to afford postgeometry optimized bond lengths in cyclometalated iridium-based complexes that are similar to those of their associated crystal structure determination.[28] The LANL2DZ and 6-31g(d) basis sets were also selected on the basis of their *a priori* successful application to the ground- and excited-state computational modeling of OLED iridium-based phosphors.[28−30]

In the case of **3**, the lowest triplet excited-state structure was also calculated using the crystal structure as a starting point for geometry optimization wherein a triplet spin multiplicity was imposed at the PBE0/LANL2DZ/6-31G(d) level of theory, following the work of De Angelis and co-workers.[29]

Frontier highest-occupied molecular orbitals (HOMOs) and lowest unoccupied molecular orbitals (LUMOs) were calculated for **1**–**7** using the LANL2DZ/6311+G(d) basis set combination and PBE0 functional. The resulting Kohn−Sham HOMO energies compared well with experimental ionization energies, as derived from oxidation potentials measured via cyclic voltammetry.[13] As such, the orbitals for each compound can be compared with each other and used for estimating the LUMO energies from TD-DFT calculations.

TD-DFT vertical excitation energies were calculated for **1**–**7** using the LANL2DZ/6311+G(d) mixed basis set with the Becke three-parameter and Lee−Yang−Parr hybrid functional (B3LYP).[31,32] B3LYP was used instead of PBE0 since it has been shown to provide excitation energies that are in better agreement with experiment for transition-metal complexes.[29]

The first six vertical singlet−singlet and singlet−triplet excitations were calculated. The two singlet−singlet transitions showing the most appreciable oscillator strength (>0.01) compared well with the

Table 1. Details of Crystal, Data Collection, and Structure Refinement for Compounds 1−7^a

	1	2	3	4	5	6	7
R1	CF$_3$	Me	F	H	H	OMe	CF$_3$
R2	H	H	H	F	H	H	H
L - X	acac	acac	acac	acac	Acac	acac	pic
FW	847.84	739.89	747.82	747.82	711.83	771.89	886.83
crystal system	orthorhombic	orthorhombic	orthorhombic	monoclinic	monoclinic	monoclinic	orthorhombic
space group	Pbca	Pbca	Pbca	P2$_1$/n	Cc	P2$_1$/n	P2$_1$2$_1$2$_1$
a (Å)	12.449(3)	10.08770(10)	17.1215(2)	11.78520(10)	20.01070(10)	10.8570(2)	16.951(3)
b (Å)	17.904(4)	18.2730(2)	17.2024(2)	21.8859(2)	63.6177(6)	16.1514(4)	17.985(4)
c (Å)	27.691(6)	30.8642(3)	18.1350(3)	21.4317(2)	17.7788(2)	17.1152(4)	21.263(4)
α (°)	90	90	90	90	90	90	90
β (°)	90	90	90	97.2931(5)	106.1941(4)	106.9820(14)	90
γ (°)	90	90	90	90	90	90	90
V (Å^3)	6172(2)	5689.28(10)	5341.32(12)	5483.15(9)	21735.0(3)	2870.38(11)	6482(2)
Z	8	8	8	8	32	4	8
Z′	1	1	1	2	8	1	2
D$_c$, (Mg/m^3)	1.825	1.728	1.860	1.812	1.740	1.786	1.813
abs coeff, mm^{-1}	4.533	4.874	5.203	5.069	5.100	4.840	4.323
F(000)	3296	2912	2912	2912	11136	1520	3432
crystal size (mm^3)	0.2 × 0.1 × 0.1	0.18 × 0.14 × 0.07	0.30 × 0.23 × 0.07	0.14 × 0.10 × 0.10	0.17 × 0.16 × 0.15	0.18 × 0.14 × 0.14	0.20 × 0.10 × 0.10
θ range (°)	2.12 to 27.47	3.32 to 27.50	2.80 to 27.49	3.17 to 27.49	5.10 to 27.21	1.77 to 27.49	3.53 to 22.20
index ranges	−15 ≤ h ≤ 16	−13 ≤ h ≤ 13	−17 ≤ h ≤ 22	−15 ≤ h ≤ 15	−24 ≤ h ≤ 24	−14 ≤ h ≤ 13	−18 ≤ h ≤ 18
	−18 ≤ k ≤ 23	−23 ≤ k ≤ 23	−20 ≤ k ≤ 22	−28 ≤ k ≤28	−53 ≤ k ≤ 80	−20 ≤ k ≤ 20	−19 ≤ k ≤ 19
	−31 ≤ l ≤ 35	−40 ≤ l ≤ 40	−23 ≤ l ≤23	−25 ≤ l ≤ 27	−20 ≤ l ≤ 21	−22 ≤ l ≤ 22	−21 ≤ l ≤ 22
reflections collected	48562	37810	33569	50242	56321	17246	37378
independent reflections	7033 [R(int) = 0.0556]	6491 [R(int) = 0.0679]	6111 [R(int) = 0.0573]	12545 [R(int) = 0.0773]	33044 [R(int) = 0.0419]	6558 [R(int) = 0.0611]	8129 [R(int) = 0.0488]
max and min transmission	0.635 and 0.538	0.7266 and 0.4741	0.7124 and 0.3046	0.6311 and 0.5372	0.5151 and 0.4777	0.5506 and 0.4762	0.6717 and 0.4785
data/restraints/ parameters	7033/0/415	6491/0/365	6111/0/365	12545/0/721	33044/2722/2754	6558/0/384	8129/100/873
GOF on F^2	1.023	1.041	1.033	1.016	1.052	1.027	1.048
R indices [I > 2σ(I)]	R$_1$ = 0.0376, wR$_2$ = 0.0827	R$_1$ = 0.0347, wR$_2$ = 0.0782	R$_1$ = 0.0313, wR$_2$ = 0.0688	R$_1$ = 0.0470, wR$_2$ = 0.0911	R$_1$ = 0.0473, wR$_2$ = 0.0903	R$_1$ = 0.0417, wR$_2$ = 0.0769	R$_1$ = 0.0273, wR$_2$ = 0.0555
R indices (all data)	R$_1$ = 0.0592, wR$_2$ = 0.0926	R$_1$ = 0.0580, wR$_2$ = 0.0884	R$_1$ = 0.0513, wR$_2$ = 0.0782	R$_1$ = 0.0805, wR$_2$ = 0.1036	R$_1$ = 0.0629, wR$_2$ = 0.0981	R$_1$ = 0.0717, wR$_2$ = 0.0884	R$_1$ = 0.0329, wR$_2$ = 0.0583
largest diff peak and hole, e·Å^{-3}	1.815 and −1.080	1.768 and −1.443	1.248 and −1.555	1.283 and −1.784	1.808 and −1.624	2.109 and −1.316	0.858 and −0.560

^{a}Common parameters: Data collection temperature, 180(2) K; wavelength, 0.71073 Å; refinement method, full-matrix least squares on F^2; absorption correction, semi-empirical multiple scans (SORTAV).

experimental UV/vis peak absorption data found by Laskar and Chen;[13] 7 showed the largest deviation of only ∼0.1 eV (see SI, Table S3). Given that the use of a hybrid functional such as B3LYP can afford such deviations as large as 0.4 eV,[29] this result shows a high suitability of the chosen basis set for these optical excitation predictions.

In all calculations, frequency checks were performed after each geometry optimization to ensure that minima on the potential energy surfaces were found. Solution-based conditions were emulated throughout, with solvent effects being incorporated via the polarizable continuum model (PCM) within a dichloromethane dielectric medium.[33,34] Given the emphasis of this paper on solid-state optical excitations, complementary solid-state calculations were also explored using a plane-wave basis set;[35] however, the large unit cells associated with 1−7 rendered extremely slow convergence, to the point that such calculations were halted in favor of the solution-based calculations presented herein. Indeed, this solution-based linear combination of atomic orbitals (LCAOs) approach is wholly consistent with all other known DFT and TD-DFT studies on cyclometalated iridium-based complexes.[36−40] Moreover, the LCAO approach is advantageous in its localization of electrons into orbitals which correspond directly to the MLCT and π−π* transitions that this study probes specifically. Furthermore, the level of difference anticipated between solid-state

and solution-based effects can be inferred indirectly for 1−7 via a comparison of each geometry-optimized DFT-generated molecular structure with that derived from the respective crystal structure. The root-mean-square deviation (RMSD) of the conformational overlay of these two molecular structures quantifies this difference,[41,42] affording an RMSD of 0.234 Å on average, across a range, 0.124−0.352 Å.

RESULTS AND DISCUSSION

Description of Crystal Structures. The molecular structures of 1−7 are shown in Figure 2.

In all cases, the iridium(III) ion resides in a distorted octahedral geometry, as expected given the bidentate nature of all of the ligands. In every compound, the two Ir−N bonds are *trans* to each other. The two benzylthiazole groups are therefore mirrored to a large extent, while the spectator ligand lies in between. The substitution of acac for pic in compound 7 results in a ∼10° smaller spectator ligand bite angle; so pic is less bulky than the acac ligand.

Overall, the iridium coordination geometry is as expected, with the exception of compound 4. There, Ir−O(2) bonds in both residues (Z′ = 2) are significantly shorter than those in the
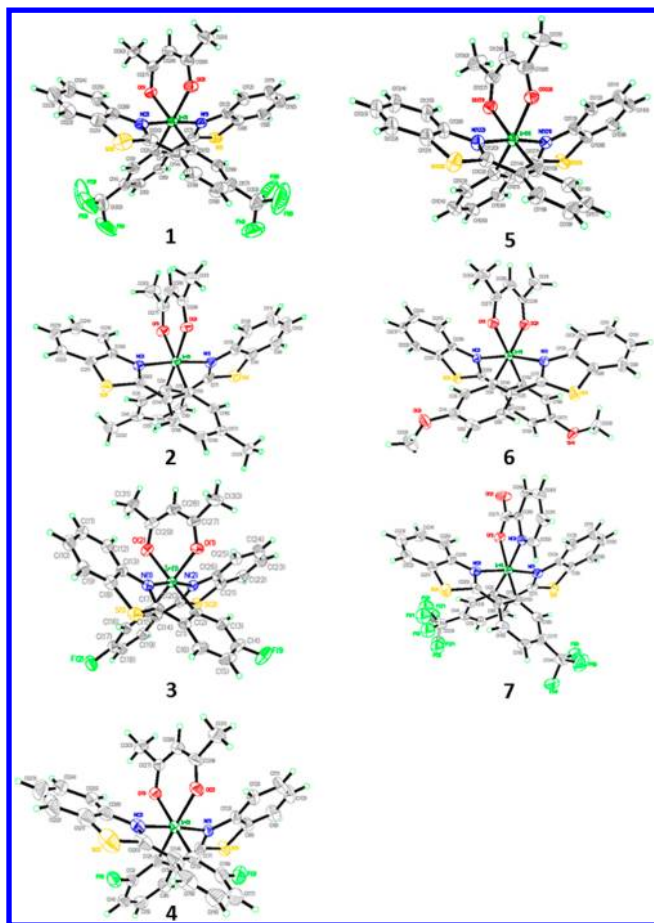
Figure 2. The crystal structures of compounds **1**–**7**. Displacement ellipsoids are drawn at 50% probability level for non-hydrogen atoms, while hydrogen atoms are shown as small spheres of arbitrary radii. For compounds **4**, **5**, and **7**, where there is more than one molecule in the asymmetric unit, only one is displayed for reasons of clarity. In such cases, the crystallographically independent molecules possess very similar geometry, except that **4** and **7** display optical isomers of each other.
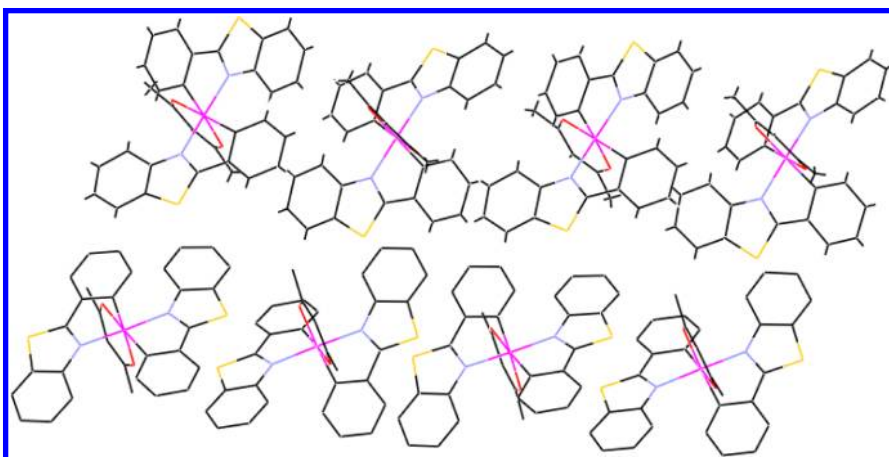
compound in this study where substitution occurs *meta* to the thiazole point of substitution (i.e., R2 ≠ H).

The structural effect of substituting fluorine at R2 rather than at R1 can be evaluated directly via a comparison of **3** and **4**. In **3**, the π-conjugation is heavily concentrated in the four phenyl bonds that are closest to the fluorine substituent. The π-electron density in the two remaining bonds in the phenyl group is correspondingly diminished. π-conjugation is extended via the presence of excess π-electron density in the bond that bridges the phenyl and thiazole groups, cf. bridging C1−C7 and C14−C20 bond lengths in **3** [1.425(6) and 1.436(6) Å] which are the shortest such bonds in all compounds studied. The nature of this π-electron distribution stands to reason given the highly electron withdrawing fluorine substituent.

Compound **4** displays a much greater demarcation of localized π-electron density than does **3**. Significant excess π-conjugation vicinal to the fluorine substitution is observed as one would expect. But an even more concentrated localization of π-electron density lies one bond apart from this π-conjugation: C5−C6 and C18−C19 bond-lengths in each molecule in the asymmetric unit [molecule #1: 1.368(10) Å, 1.355(13) Å; molecule #2: 1.369(11) Å, 1.385(9) Å] are very short, given the ostensible aromatic nature of a phenyl ring. In common with **3**, π-conjugation extends into the phenyl-thiazole bridging bond of one of the two molecules in the asymmetric unit of **4**, but not the other; overall, this π-conjugation extension is slight relative to that observed in **3** [cf. molecule #1 of **4**: C1−C7, 1.447(9) Å; C14−C20, 1.435(11) Å; molecule #2 of **4**: C1−C7, 1.453(9) Å; C14−C20, 1.447(9) Å]. While these π-electron density localization effects are pronounced in **3** and **4**, there is no clear evidence of any similar effects ensuing in the other compounds. This corroborates the notion that these localization effects are due to the presence of the very electron-withdrawing fluorine substituent.

Considering the thiazole part of the bt ligand, there is a significant level of π-electron density between the N and S atoms in all compounds. The phenyl part of this thiazole unit exhibits aromatic character, although the bond distances reveal a tendency toward localization in the bonds one apart from the ring fusing bond; cf. C9−C10, C10−C11, C22−C23, and C24−C25 bond lengths (see Supporting Information) which are generally shorter than the others in this phenyl ring, most notably so for the C9−C10 bond in **4** [1.357(11) and

other compounds. Furthermore, its C−Ir−N bite angles are noticeably large [96.7(2)−99.1(2)°] compared with 90.2(2)−97.2(3)°]. These features may be attributed to the steric or electronic effects of the fluorine group, noting that **4** is the only

Figure 3. The asymmetric unit of **5**, illustrating the different orientations of the molecules in the two rows.

1.359(12) Å]. This further evidence of localization of π-electron density in **4** is noteworthy.

The opportunity for charge-transfer between the thiazole and phenyl rings was assessed by considering the twist angle between them. The rings in **2**−**6** forge an angle with respect to each other in the range 4.5−11.9(10)°; that these rings are nearly planar to each other shows that charge-transfer is largely unaffected by the nature of the substituent. Such ligand geometry is typical of that in related compounds.[13] The rings in compounds **1** and **7** are more distorted, with twist angles up to 18.3(9)° and 15.6(8)°, respectively. This distortion is presumably steric in origin given the bulky and disordered CF$_3$ substituent which is common to both of these compounds. This hypothesis is substantiated by the observation that **6** contains the next most bulky (albeit ordered OMe) substituent and displays the next highest twist angle (11.9(8)°). Further evidence of CF$_3$ steric hindrance is given by the angle between the mean planes of the two phenyl-benzothiazole ligands in compound **1** which is significantly more acute than the same in **2**, **3**, **4**, **6**, and **7**; cf. 70(1)° with 78−88(1)°, respectively.

Compound **5** was not included in this comparison since there are eight molecules in its asymmetric unit ($Z' = 8$); so such angles will be influenced by a very different molecular environment. These eight molecules arrange themselves in two columns of four molecules, with neighboring molecules being optical isomers of one another (Figure 3). Compounds **4** and **7** also display their respective optical isomers in the solid-state, albeit with only two molecules in the asymmetric unit ($Z' = 2$).

The supramolecular environment in **1**−**7** was also investigated. C−H⋯F hydrogen bonds were identified in **3**, **4**, and **7**: C5−H5⋯F2 [H⋯F: 2.378 Å, 157.46°, 0, 1/2 + 2y, 1/2] in **3**; C16−H30A⋯F1A [H⋯F: 2.420 Å, 131.52°, 1, 0, 0] involving one symmetric unit of **4**; C13−H23B⋯F1B [H⋯F: 2.301 Å, 125.70°, 1/2 + x, y, −1/2 + z] and C19−H19B⋯F2b [H⋯F: 2.432 Å, 148.08°, 1/2 + x, y, −1/2 + z] involving the other asymmetric unit of **4**; C6_1-H6A_1⋯F4_1 [H⋯F: 2.452 Å, 157.68°, 1/2, −1 1/2 + 2y, 2z] in one asymmetric unit of **7**. Compound **5** displays two types of intermolecular interactions: C620−S602⋯C529 [S⋯C: 3.185 Å, 162.77°, 1, 0, 0] and C829−S501⋯C507 [S⋯C: 3.219 Å, 163.23°, 1/2, 1/2, 0]. No abnormally short nonbonded contacts were found in **1**, **2**, and **6**. Nor were any appreciable π⋯π interactions found in any of the compounds; despite the abundance of conjugated rings in these molecules, they are at best poorly overlapped.

Overall, the intermolecular interactions observed are all weak, considering the nature of the atoms involved and the length of the interactions. However, given the absence of stronger interactions, they are likely to influence significantly the crystal packing due to their cooperative nature.

Photophysical Properties. In order to assess the emissive properties of **1**−**7**, UV/vis absorption spectra are required as a prerequisite. Such measurements on compounds **1**−**6** were obtained previously in the solution state,[13] but that for **7** was unknown prior to this study.

The solution-state UV/vis absorption spectrum of compound **7** was therefore undertaken, which revealed very similar spectral features with the following band maxima and extinction coefficients (λ_{abs}/nm (ε/10^{-4} dm^3 mol^{-1} cm^{-1})): 254 (3.30), 294 (2.92), 314 (3.03), 328 (3.12), 358 (1.06), 392 (0.75), 436 (0.62).

Given the similarity to that observed by Lasker and Chen,[13] this shows that intraligand (IL) π−π* transitions, triplet and singlet metal-to-ligand charge transfer (^{3}MLCT and ^{1}MLCT)

transitions are all present in the solution-state of all seven complexes at room temperature. An admixture of these charge-transfer states dominates the overall absorption character, although IL transitions are exclusively responsible for the absorption profile below ∼350 nm. Above this wavelength, IL and MLCT mixing occurs until ∼385 nm, where ^{3}MLCT and ^{1}MLCT mixing begins; this is apparent in the range, λ = 385−450 nm and involves spin−orbit coupling with the Ir(III) ion.

Solid-state emission spectra were then obtained from single-crystals of compounds **1**−**7**, at temperatures of 100 and 298 K, and are presented in Figure 4b,c, respectively. For comparison purposes, analogous room temperature solution-state emission spectra were also collected (Figure 4a). Corresponding $\lambda_{emission}$ peak centers and emission lifetimes at each temperature are given in Table 2.

In common with analogous solution-state emission spectra, a broad emission envelope was observed for compounds **1**−**7** in the solid-state at both 100 and 298 K. The solid-state emission envelope is, however, much more structured than the solution-state spectra. A more pronounced, sharper vibrational structure stems from the more rigid and defined solid-state structure. Furthermore, while there is little to discern between compounds **1**−**7** in the solution-state, with the exception of the changing position of λ_{max}, solid-state emission profiles are quite diverse.

Complexes **1**, **2**, **4**, and **5** present three well-resolved peaks. Four peaks are discernible for compounds **6** and **7**; hints of the fourth feature are implied in **1**, **2**, **4**, and **5** from small shoulders of the discernible peak at highest wavelength. Four peaks manifest in the spectrum for **3** as well, although its profile is notably more diffuse than that of all of the other compounds.

These features represent the various charge transfer states already discussed when describing the absorption spectra. The ^{3}MLCT state, giving the higher absorption wavelength, is a spin-forbidden transition. Its spectral contribution therefore has a markedly diffuse nature. Mixing of ^{1}MLCT and ^{3}MLCT states will further broaden the spectral features.

2 shows the greatest distinction between individual electronic transitions. In particular, the IL charge-transfer (centered around λ = 550 nm) is the most pronounced of all complexes studied; its peak isolation indicates that there is little IL and MLCT mixing in this compound. **2** is also the only complex with an electron donating R1 substituent (Me). Given that R1 is *meta* to the Ir metal which is also electron donating, one expects the least MLCT from this compound. Indeed, its MLCT band is the most red-shifted across all spectra, to the extent that this spectrum displays the greatest bandwidth of all profiles.

3 has by far the most diffuse spectral profile. It contains the most electronegative R1 substituent (F). The effect of F substitution at a position *meta* or *para* to the thiazole bridge could also be assessed by spectral comparison of **3** and **4**. The peak maxima appear at similar wavelengths; yet, the spectrum for **4** displays much more MLCT and a more well-defined spectral profile. The explanation for these features is 2-fold. The *ortho* correspondence of R2 and the Ir ion offers superior MLCT opportunities. Meanwhile, the more structured spectrum of **4** is expected since the R2 position affords much more localized features of π-conjugation than in **3**, as revealed herein by the crystal structure analysis. In contrast, since R1 is *para* to the thiazole bridge, **3** displays a more pronounced and widespread electron-withdrawing character, as shown earlier via
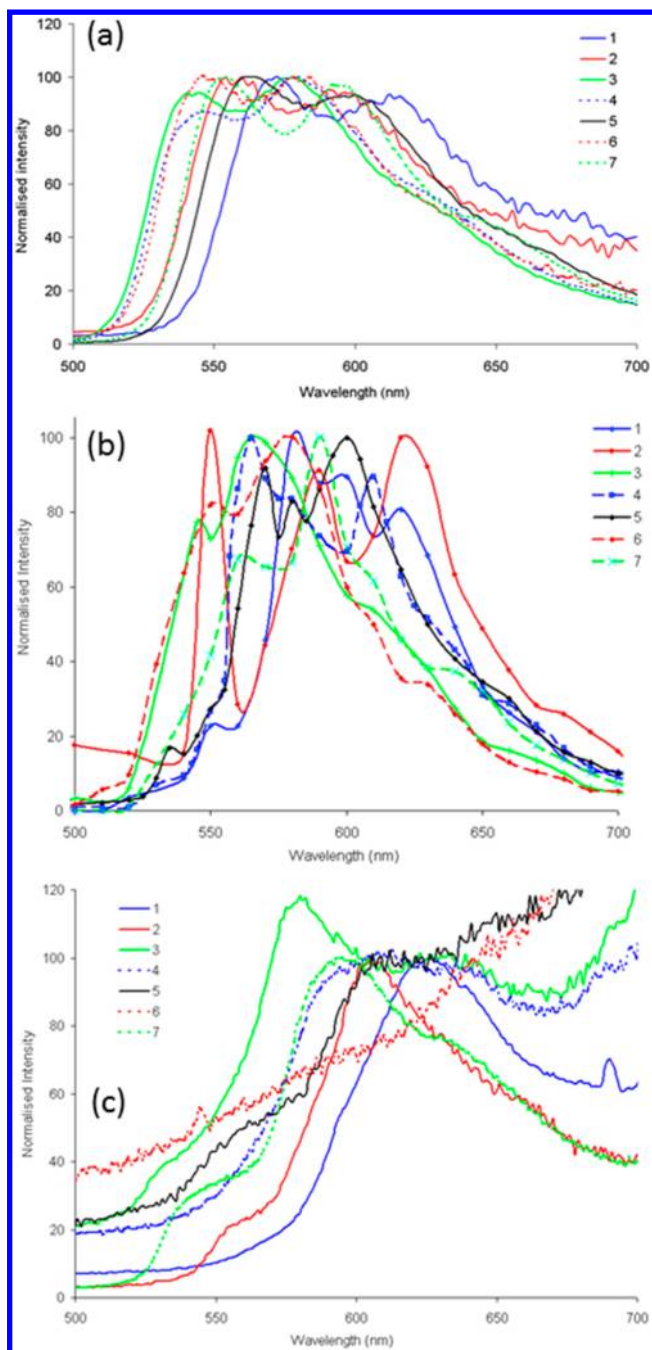
Figure 4. Normalized emission spectra (λ_{exc} = 355 nm) of **1−7** in (a) CH$_2$Cl$_2$ solution and crystalline samples at (b) 100 K and (c) 298 K. Concentrations for solutions were **1**, 2.36 × 10^{-4} M, **2**, 5.41 × 10^{-4} M, **3**, 5.38 × 10^{-4} M, **4**, 4.68 × 10^{-4} M, **5**, 4.886 × 10^{-4} M, **6**, 5.18 × 10^{-4} M and **7**, 4.521 × 10^{-4} M.

Table 2. Solid (Crystalline) State Emission Data for Crystalline 1−7 at 298 K and at 100 K

	$\lambda_{emission}$ /nm (λ_{exc} = 355 nm)[b]		$\tau_o/\mu s$[c]	
compound	298 K	100 K	298 K	100 K
1	575, 629[a]	550, 580[a], 620	1.7	1.5
2	560, 605[a], 660	570, 610[a], 660	1.5	1.4
3	535, 580[a], 635	570[a], 610	2.3[d]	3.1
4	610[a], 640	565[a], 610, 640	0.3	1.4
5	570, 610[a]	570, 580, 600[a], 660	1.7	3.4
6	600, 650[a]	550, 580, 630[a]	2.4	4.0
7	545, 595[a], 635	570, 590[a], 610, 640	1.5	2.5

[a]Denotes peak with maximum emission. [b]The emission spectra at 298 K gave only broad envelopes, and thus selecting the wavelength at the peak maximum involved a large margin of error (±10 nm). Because of the resolution limits of the data collected at 100 K, the wavelengths have an error ± 5 nm. [c]Lifetimes have an error of ±20%. [d]This measurement was at 260 K.

CF$_3$ environment. Indeed, the structural analysis of **1** has already revealed that the CF$_3$ group exhibits molecular disorder and that this is dynamic in nature.

Considering the effect of no substitution (i.e., R1, R2 = H), the various λ_{max} values for complex **5** reside at similar positions to those of compounds **3** and **6**, while its spectral profile is markedly different to those spectra. The spectrum reveals a distinct structure with three discernible peaks, the intensity ratios of which are most like compound **2**, but the breadth of the overall spectra is akin to compound **1**. These considerations imply that its charge-transfer characteristics are the same in nature to those that dominate in compound **2**; this is expected since R1 is electron donating in both cases. Yet, there is an electronic band-narrowing of the electronic states for **5** relative to that in compound **2**. Indeed, the charge-transfer bandwidth appears more akin to that of the complexes where R1 is an electron-withdrawing group. A possible explanation for these observations is that the bt rings in **5** are substantially distorted, when averaged over the solid-state, given the finding that there are eight molecules in the asymmetric unit. The bt distortion will disrupt IL charge-transfer. Moreover, the opportunities for IL transitions will be naturally diminished since IL transitions require well-defined energy levels rather than this eight-way spread, cf. the red shift of the IL peak. A corresponding blue shift of the MLCT transitions will effect an overall bandwidth narrowing. Such a blue shift stands to reason given that the spin-forbidden nature of ^{3}MLCT transitions makes them energy diffuse; so they are best able to accommodate a range of energy levels from the eight different bt ligands in the asymmetric unit.

The effect of replacing the spectator ligand, acac, with pic was investigated by comparing spectra for compounds **1** and **7**. The spectral profile of **7** is markedly more diffuse than that of **1**, which implies that there is more mixing of different charge transfer states in **7**. The more distorted bt ligands in **1** may partially account for this difference. The spectral profiles of **1** and **7** have four similar features, but the λ_{max} values in **1** (Table 2) are markedly red-shifted relative to **7**. This suggests that more charge-transfer prevails in **7** than in **1**. The lower bite angle of pic versus acac may be an influential factor in this regard since the competition for steric effects over electronic effects will be reduced relative to that in **1**.

Comparison of 100 and 298 K spectra (Figure 4b,c, respectively) demonstrate a striking loss of emission in the

the structural analysis. The more extended π-electronic delocalization that results causes the more diffuse spectrum.

The sequential effect of varying electronegativity in the substituents (F > CF$_3$ > OMe) could be assessed by comparing spectra for **3**, **1**, and **6**, respectively. Spectra of **3** and **6** are similar, with **6** slightly red-shifted relative to **3** as one would expect given the lower electronegativity of OMe, which results in less charge-transfer. The spectral profile of **1** is, however, markedly red-shifted relative to both of these comparison spectra and is distinctly more structured. This extra spectral structure implies that vibronic contributions may arise from this

area associated with IL charge-transfer at room temperature. Only a hint remains as a shoulder for **2**, **3**, **5**, and **7** at 298 K; in others it is entirely absent. The broad envelope revealed at 298 K in all compounds except for **6** is centered in the region characteristically linked to MLCT transitions. The nature of the emissive state for compound **6** appears to have been completely altered and no electronic transitions are resolvable.

The solid-state excited-state lifetimes of **1**−**7** (Table 2) are all several microseconds at 100 K. This time frame indicates that ^{3}MLCT character dominates the emissive state. The lifetimes either remain the same within experimental error (**1**, **2**) or slightly diminish at 298 K (**3**−**7**). The slight diminutions for **3** and **5**−**7** are expected given that lifetimes generally decrease with increasing temperature due to thermal deactivation pathways. A significant decrease in emission lifetime, however, suggests a diminution of ^{3}MLCT character with increasing temperature. Such a change is significant for **4**, where the lifetime decreases by almost an order of magnitude at 298 K; indeed, this lifetime (τ_0 = 300 ns) is also the only one that is less than a microsecond. Our rationale for this exception pertains to the key discriminatory feature of **4** from all of the other six compounds in that it has a non-hydrogen substituent at R2. As mentioned earlier, substitution of F at the R2 position deters the extended π-electron delocalization somewhat, offering intrinsically less options for charge-transfer. This hypothesis is corroborated by the fact that **4** is identical to **3** with the exception of the position of the F substituent in the phenyl ring, and yet **3** displays lifetime characteristics that are common to all other compounds.

Photo-Excited Intramolecular Charge-Transfer and Optical Band Gap Calculations. Complementary DFT calculations support the photophysical findings of **1**−**7** in terms of MLCT and IL charge-transfer characteristics. DFT-generated frontier molecular orbitals are displayed in Figure 5.[43] The iridium and two juxtaposing phenyl moieties dominate the charge-transfer characteristics in the HOMO, leaving the benzothiazole units essentially bare. In stark contrast, the charge-density distribution is generally much more even in the LUMO and LUMO+1, demonstrating that the primary nature of intramolecular charge-transfer owing to UV/vis absorption concerns the benzothiazole units, both in the context of π−π* optical transitions and their interaction with the iridium center via MLCT. The LUMO and LUMO+1 are in fact nearly identical for **1**, **2**, **3**, and **5**. Those for **4**, **6**, and **7** show some contrast which is presumably a manifestation of their noticeable differences in orbital energies (see SI, Figure S1).

TD-DFT reveals that the highest oscillator strengths vary in their origin, either as a HOMO−LUMO transition (for **5**−**7**) or a HOMO−LUMO+1 transition (**1**−**4**). With that said, the LUMO and LUMO+1 energy levels lie very close to each other in the solution state (see SI, Figure S1) and so could readily switch when considering the solid-state photophysics. The lowest-lying HOMO energies correspond to **1** and **7**, whereas the highest relate to **2**, **5**, and **6**. Considering that **2**, **5**, and **6** are the only compounds in this series that do not contain a fluorine substituent, the presence of fluorine can be seen to lower the HOMO energy level. The TD-DFT-derived optical band gap (LUMO−HOMO) is overestimated for all compounds, as is expected for such DFT calculations. However, the successive blue-shifting trend in the optical band gap (**1** < **5** < **7** < **2** < **4** < **6** < **3**) is the same as that observed by experiment.[13]

Implications of Results for Photocrystallography Experiments. The structure−property relationships that
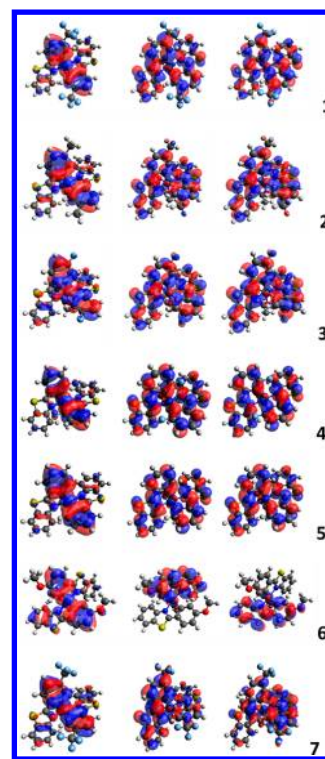

Figure 5. HOMO, LUMO, and LUMO+1 representations of **1**−**7**, drawn at the 0.02 isosurface level.

have unfolded from the discussion above represent results in their own right. Yet, in addition, the findings from these crystal structure determinations and photophysical measurements serve to assess the suitability of compounds **1**−**7** for a time-resolved stroboscopic (optical)pump-(X-ray)probe photocrystallography experiment, designed to realize the 4-D (space-time) resolved photoexcited state structure of the compound. The bond geometry of the transient ^{3}MLCT state is of particular interest since it is this state that most affects the optoelectronic properties. Prior assessment of the compounds is necessary because of the significant technical challenges such experiments present; indeed, it is important to realize that not all materials can be studied by photocrystallography, because certain intrinsic optical or structural characteristics of a material can preclude its viability, at least at the current stage of technical development.

The suitability of a material for photocrystallography can be assessed via the sequential decision-making process described in the flow diagram of Figure 6. For each material candidate, the decisions are informed by querying certain aspects of the structural and photophysical property results (indicated in green, Figure 6, left and right columnar flows, respectively).

Evidently, a viable sample candidate must exhibit a photoinduced structural change that would be large enough to resolve crystallographically. In order to discern this, the intrinsic physical origin of this photostructural change needs to be categorized into one of the various types.[44] Therein, UV/vis absorption spectroscopy measurements are employed (Figure 6, right columnar flow). In this case study, these demonstrate that the MLCT process occurs in the long-wavelength part of the UV/vis spectral profile. From a photostructural point of view, an accompanying change in the metal-to-ligand separation due to this ^{3}MLCT transition would be expected. Such ΔM-L
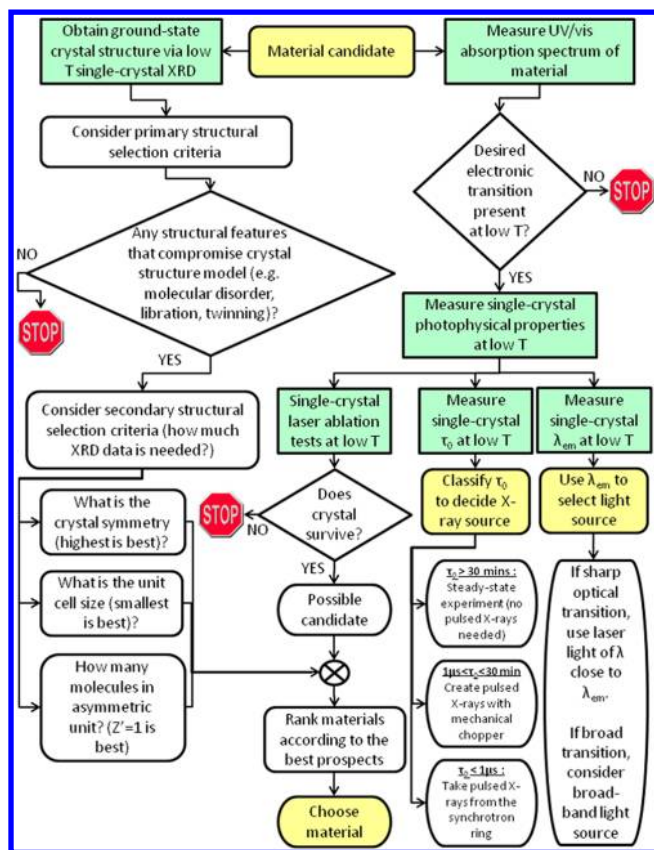
Figure 6. Flow diagram of the decision-making process followed in order to select a viable compound for a photocrystallography experiment. The start and end points of the overall process are highlighted in yellow. The green boxes resemble measurements.

perturbations are likely to be of the order of 0.1−0.2 Å, based on previous work.[45−51]

The UV/vis absorption spectrum also pinpoints the optimal photoexcitation wavelength region to observe this [3]MLCT transition. It is noteworthy to add that while phosphorescence usually affords low photoconversion levels, this iridium family of compounds demonstrates unusually high optical quantum-yields; indeed, it is this photophysical property attribute that renders their favorable exploitation as phosphors in OLEDs.[1,3−5] The atomic resolution of the metal-to-ligand separation perturbation that is sought needs to be optimized. Photocrystallography measurements are typically undertaken at nitrogen-based cryogenic temperatures in order to minimize atomic vibrations. So low temperature UV/vis emission spectroscopy on a single-crystal sample was employed to check that the photostructural change persists under the sample conditions that a photocrystallography experiment would be conducted.

The associated lifetime of the desired optical transition, τ_0, also needs to be realized in order to enable one to design the technical aspects of the experiment; in particular, τ_0 determines which type of light (pump) and X-ray (probe) sources to use, if a photocrystallography experiment turns out to be feasible from the materials-centered perspective. Since the single-crystal UV/vis emission lifetimes of complexes **1−7** range from 1.4(3) to 4.0(8) μs at 100 K (Table 2), τ_0 for all complexes fall within the $1\ \mu s < \tau_0 < 30$ min classification presented in Figure 6. Time-resolved X-ray pulses can therefore be produced via a mechanical chopper.[52−55] Given the low duty cycle associated

with the resulting X-ray beam, the concerted use of a synchrotron source in multibunch mode, or similar, is strongly recommended for such experiments so as to ensure adequate X-ray intensity.

The choice of light source is informed by the absorption and emission profiles associated with the [3]MLCT transition. A $\lambda_{excitation}$ of 355 nm was chosen for the UV/vis emission spectroscopy of **1−7** in order that each complex could be optically pumped in a spectral region which featured MLCT character and yet had relatively low optical absorbance.[13] Choosing a low absorbance maximizes the optical penetration depth of a sample[16] so that the single-crystal for a photo-crystallography experiment can be as large as possible, to maximize X-ray diffraction intensities, within the limit of its optical density at the optical pump wavelength. While an $\lambda_{excitation}$ of 355 nm is associated with a mixed IL/MLCT character, the [3]MLCT and IL transitions can be discriminated via the microsecond time-resolved nature of the prospective photocrystallography experiment; [3]MLCT phosphorescence affords these microsecond lifetimes. For photocrystallography experiments, one must also consider if a single-crystal will survive sustained exposure to the light source employed. During the course of these spectroscopy measurements, single crystals of a range of sizes (∼0.1−0.5 mm) were exposed to the 355 nm laser light (0.2 mJ/pulse) and were found to be stable even when laser exposures lasted >2 h. This is an important laser ablation time threshold since it corresponds to a typical synchrotron data acquisition time frame, indicating that a crystal of any of these subject complexes will survive the duration of a photocrystallography experiment. As such, all complexes **1−7** meet the photophysical properties selection criteria for photocrystallography, as set out in the right-hand columnar flow of Figure 6.

One also needs to assess if there is any feasible discrimination in the material candidates on the basis of ground-state crystal structure attributes. The left path of the flow diagram in Figure 6 is thereby considered. The material selection criteria in this decision-making line are slightly different in design to those which concern the photophysical properties. Here, only one measurement is required: the determination of the ground-state crystal structure of complexes **1−7** via low temperature single-crystal X-ray diffraction. Decision-making associated with the crystal structure results is divided into primary and secondary material selection criteria. The primary criteria impose a mandatory knockout if the material does not meet the required conditions. The secondary criteria are best thought of as conditions that facilitate a photocrystallography experiment. As such, if there is more than one option after considering primary selection criteria, one can shortlist a series of materials upon the basis of these conditions. Yet, within reasonable limits of these secondary selection criteria, a photocrystallography experiment is still possible, at least in principle, if one were to choose any material option.

Concerning primary selection criteria, the ground-state must not feature any *nonphotostructural* complications, e.g., twinning, disorder, or libration effects, since nonphotostructural effects could obscure the subtle photostructural features sought and would compromise resolution of the structural data. Considering compounds **1−7** in this context, **1** and **7** are not viable for photocrystallography experiments owing to the molecular disorder in their CF_3 groups. From the sole perspective of nonphotostructural effects, there appears to be nothing to hinder a photocrystallography experiment on **2−6**.
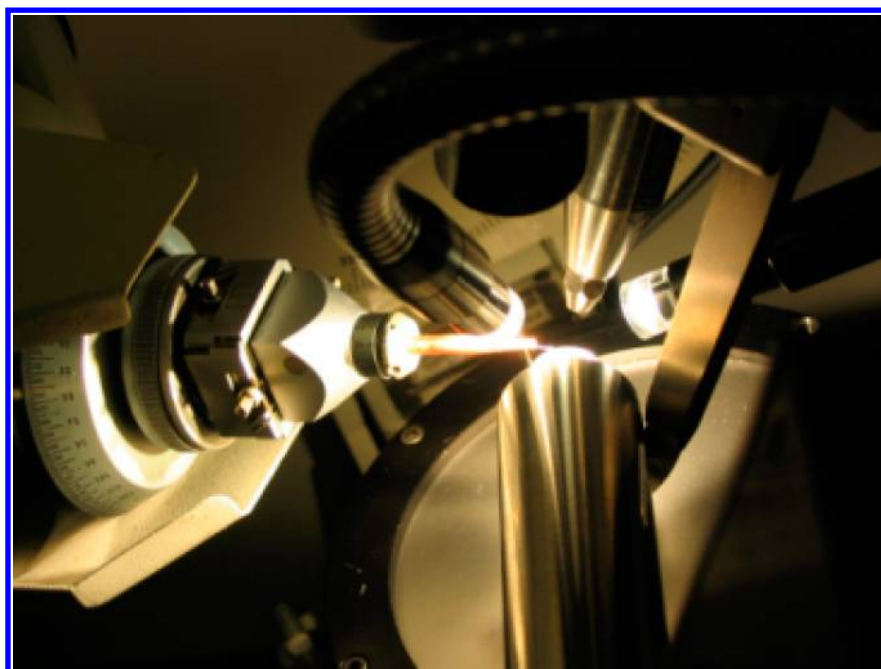
Figure 7. A typical experimental setup of a photocrystallography experiment. The compactness of ancillary equipment that surrounds the sample is illustrated. The single-crystal sample is located on the (right-hand) end of an optical fiber which is lit up in the center of the photo.

Concerning the secondary selection criteria, one is essentially considering the technical demands on a photocrystallography experiment that are imposed by the *photostructural* effects in a given material. These pertain to practical data acquisition challenges imposed by the photoinduced process. For example, the crystal symmetry, unit cell size, and number of molecules in the asymmetric unit (Z') of a crystal structure will have a fundamental impact on the data-collection time requirements of a photocrystallography experiment and the data-to-parameter ratio of an associated structural refinement. A low crystal symmetry could also impose practical challenges associated with the geometry of ancillary equipment that is required for a photocrystallography experimental setup. An illustration of a typical experimental setup is provided in Figure 7, showing the compactness of such equipment around a sample. This imposes a physical blocking of certain parts of the Ewald sphere; i.e., the possible data coverage of reciprocal space coverage is somewhat compromised.

Bearing all of this in mind, a material presenting a technically easy situation would feature high crystal symmetry, small unit cell size, and a $Z' = 1$. The crystal symmetries of **1**−**7** are all either monoclinic (**4**−**6**) or orthorhombic (**1**−**3**, **7**). In addition, it was noted that the unit cell *c*-axis for **1**, **2**, and (especially) **5** is on the large side. **5** is also ruled out since it contains so many molecules in the asymmetric unit ($Z' = 8$); this would impose too many parameters on a photocrystallography refinement. The viability of compounds **4** and **7** is similarly questionable since $Z' = 2$ in each case. While one example exists of a successful photocrystallography study on a molecule with $Z' = 2$,[56] this concerned a long-lived photoinduced species, while the microsecond-lived photoexcited states of these iridium-based complexes imposes significantly higher technical demands.

The overall result of these decision-making steps affords an easy choice of **3** or **6** as superior material candidates for a photocrystallography experiment. Subsequent to this generic decision-making process, one can further fine-tune material

choices by considering the specifics of the compounds in hand. In this case study, there is a slight preference for **3** given the greater electron withdrawing group on the bt ligand compound to that of **6** (F versus OMe); as such, this will enhance charge-transfer effects. One can also consider the pros and cons of much more subtle features such as the crystal field forces which surround a molecule within a crystal lattice: can a molecule readily accommodate the anticipated photostructural change within its crystal lattice, without causing undue stress or strain? Such forces can either fracture the crystal due to the photoirradiation process,[16] or prevent the photostructural change from actually happening. Conversely, intermolecular forces can help to stabilize a photostructural change.[57] Given that the anticipated photostructural change is associated with MLCT, by far the most significant structural perturbation will occur around the iridium core. The bt ligands may be pushed outward to a minor extent, as a secondary effect, assuming a slight ricochet effect from the weakening of the affected M-L coordination. The supramolecular environment of the ground-state should therefore also be checked to see if it can accommodate and stabilize this photostructural change. Since the primary intermolecular forces are of a van der Waals nature, a slight outward perturbation of any part of the bt ligand should be viable without causing undue crystal lattice stress or strain. The aforementioned weak C5−H5···F2 intermolecular interaction in **3** (see Figure 8) could also act to stabilize the photoinduced effects since it would stand to strengthen this interaction slightly; while weak, such interactions have shown to be property dictating.[58] Meanwhile, **6** was found to have no distinguishable nonbonded contacts. Again, **3** therefore holds a slight edge over **6**.

Given the overall preference for **3**, its lowest-energy triplet excited state was calculated using DFT, in order to anticipate the precise level of structural perturbation that can be expected in association with a ^{3}MLCT optical transition. The overall conformational change in molecular structure, upon transitioning from the S_0 ground-state to triplet T_1 photoinduced state
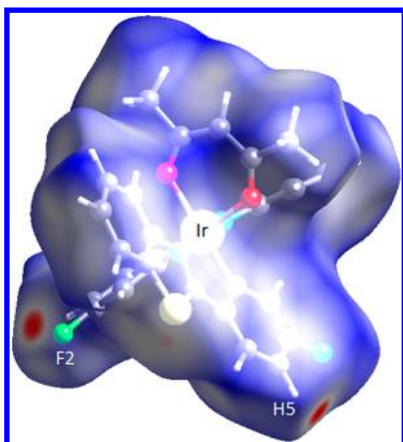
Figure 8. Hirshfeld surface of **3**. Red features illustrate the areas of closest approach to neighboring molecules; these correspond to a weak C5—H5···F2 intermolecular interaction. The otherwise lack of directed interactions shows that van der Waals forces comprise the nature of crystal field effects in **3**.

was quantified via an RMSD of 0.245 Å.[41,42] As expected, the largest individual bond perturbation is associated with the two Ir—N bonds, which manifest contractions of 0.050 Å and 0.052 Å from $S_0 \rightarrow T_1$ (SI, Table S14). Given that the experimental error associated with the experimentally derived Ir—N bond-lengths in the ground state is 0.003 Å, an average photoinduced Ir—N bond contraction of 0.051(3) Å should be readily observable. Accordingly, a microsecond-time-resolved (optical)pump-(X-ray)probe diffraction experiment on **3** will be the subject of future work.

CONCLUSIONS

This study has established solid-state structure−property relationships in a series of seven luminescent-based cyclo-metalated iridium-based complexes. Specifically, their molecular structures and solid-state photophysical properties have been compared. Chemical substitution at the bt ligand was found to cause various red- or blue-shifts according to the donor or acceptor strength of the substituent, or to the relative position of this substituent on the bt ligand. The replacement of the spectator ligand (acac to pic) results in more charge-transfer and broader profiles, presumably owing to a greater mixing of MLCT and IL states. The geometric distortion of bt was found to disrupt IL charge-transfer, especially in **5** where there is substantial variation on account of Z' = 8 in its crystal structure. Emission signatures from IL charge-transfer disappear at room temperature in **1**, **4**, and **6** and are heavily depleted in the spectra of all other complexes. Corresponding lifetimes with a λ_{exc} of 355 nm are on the order of several microseconds which is indicative of ^{3}MLCT character. These structure−property relationships are important results in their own right given their potential solid-state application as OLED material components.

The single-crystal phase was probed explicitly throughout this experimental study since one of its key goals was to prospect these materials as possible candidates for a future time-resolved (optical)pump (X-ray)probe photocrystallography experiment. Complexes **3** and **6** were found to be viable candidates, as a result of a formulated decision-making process that profiles these materials for such experiments. The seven subject complexes served as a case study to illustrate this process in detail. This process was also shown to help determine important technical requirements that dictate the

overall design of the photocrystallography experiment. This process is deliberately generic, and within that scope, the choice between **3** and **6** would be moot. However, it is shown that one can further narrow this choice to a single material, if one takes on board a comparison of these short-listed materials according to certain specifics that are unique to a given family of compounds. Accordingly, a time-resolved photocrystallography experiment of **3** will be the subject of future work. Owing to the very challenging nature of such experiments and the associated data analysis, the judicious prior selection of a material is crucial for the successful continuing development of photocrystallography.

■ ASSOCIATED CONTENT

ⓢ Supporting Information

X-ray crystallographic files in CIF format for compounds **1**−**7**. This information is available free of charge via the Internet at http://pubs.acs.org.

■ AUTHOR INFORMATION

Corresponding Author
*E-mail: jmc61@cam.ac.uk.

Present Addresses
#(A.Z.) Department of Physics, University of Bath, Bath, BA2 7AY. United Kingdom.
⊗(I.R.L.) Department of Chemistry, Birla Institute of Technology and Science (BITS), Pilani, Rajasthan, 333031. India.

Notes
The authors declare no competing financial interest.

■ REFERENCES

(1) You, Y.; Park, S. Y. *Dalton Trans.* **2009**, 1267.
(2) Balzani, V.; Scandola, F. *Supramolecular Photochemistry*; Ellis Horwood: Chichester, UK, 1991.
(3) Mak, C. S. K.; Hayer, A.; Pascu, S. I.; Watkins, S. E.; Holmes, A. B.; Köhler, A.; Friend, R. H. *Chem. Commun.* **2005**, 4708.
(4) Evans, N. R.; Devi, L. S.; Mak, C. S. K.; Watkins, S. E.; Pascu, S. I.; Kohler, A.; Friend, R. H.; Williams, C. K.; Holmes, A. B. *J. Am. Chem. Soc.* **2006**, *128*, 6647.
(5) Lamansky, S.; Djurovich, P.; Murphy, D.; Abdel-Razzaq, F.; Lee, H.-E.; Adachi, C.; Burrows, P. E.; Forrest, S. R.; Thompson, M. E. *J. Am. Chem. Soc.* **2001**, *123*, 4304.
(6) Wang, R.; Deng, L.; Zhang, T.; Li, J *Dalton Trans* **2012**, *41*, 6833.
(7) Baldo, M. A.; O'Brien, D. F.; You, Y.; Shoustikov, A.; Sibley, S.; Thompson, M. E.; Forrest, S. R. *Nature* **1998**, *395*, 151.

(8) Baldo, M. A.; Lamansky, S.; Burrows, P. E.; Thompson, M. E.; Forrest, S. R. *Appl. Phys. Lett.* **1999**, *75*, 4.

(9) Thompson, M. E.; Burrows, P. E.; Forrest, S. R. *Curr. Opin. Solid State Mater. Sci.* **1999**, *4*, 369.

(10) Neve, F.; La Deda, M.; Crispini, A.; Bellusci, A.; Puntoriero, F.; Campagna, S. *Organometallics* **2004**, *23*, 5856.

(11) Grushin, V. V.; Herron, N.; LeCloux, D. D.; Marshall, W. J.; Petrov, V. A.; Wang, Y. *Chem. Commun.* **2001**, 1494.

(12) Lamansky, S.; Djurovich, P.; Murphy, D.; Abdel-Razzaq, F.; Kwong, R.; Tsyba, I.; Bortz, M.; Mui, B.; Bau, R.; Thompson, M. E. *Inorg. Chem.* **2001**, *40*, 1704.

(13) Laskar, I. R.; Chen, T.-M. *Chem. Mater.* **2004**, *16*, 111.

(14) Cole, J. M. *Acta Crystallogr.* **2008**, *A64*, 259.

(15) Cole, J. M. *Zeit. Krist.* **2008**, *223*, 363.

(16) Cole, J. M. *Chem. Soc. Rev.* **2004**, *33*, 501.

(17) Coppens, P.; Fomitchev, D. V.; Carducci, M. D.; Culp, K. *J. Chem. Soc., Dalton Trans.* **1998**, 865.

(18) (HKLDenzo and Scalepack): Otwinowski, Z.; Minor, W. *Methods in Enzymology*, Vol. 276, Macromolecular Crystallography, Part A; Carter, C. W., Jr, Sweet, R. M., Eds.; Academic Press: New York, 1997, pp 307−326.

(19) Blessing, R. H. *Acta Crystallogr.* **1995**, *A51*, 33.

(20) Sheldrick, G. M. *Acta Crystallogr.* **2008**, *A64*, 112.

(21) Chen, L.; Yang, C.; Qin, J.; Gao, J.; Ma, D. *Inorg. Chim. Acta* **2006**, *359*, 4207.

(22) Frisch, M. J.; Trucks, G. W.; Schlegel, H. B.; Scuseria, G. E.; Robb, M. A.; Cheeseman, J. R.; Scalmani, G.; Barone, V.; Mennucci, B.; Petersson, G. A.; Nakatsuji, H.; Caricato, M.; Li, X.; Hratchian, H. P.; Izmaylov, A. F.; Bloino, J.; Zheng, G.; Sonnenberg, J. L.; Hada, M.; Ehara, M.; Toyota, K.; Fukuda, R.; Hasegawa, J.; Ishida, M.; Nakajima, T.; Honda, Y.; Kitao, O.; Nakai, H.; Vreven, T.; Montgomery, Jr., J. A.; Peralta, J. E.; Ogliaro, F.; Bearpark, M.; Heyd, J. J.; Brothers, E.; Kudin, K. N.; Staroverov, V. N.; Kobayashi, R.; Normand, J.; Raghavachari, K.; Rendell, A.; Burant, J. C.; Iyengar, S. S.; Tomasi, J.; Cossi, M.; Rega, N.; Millam, N. J.; Klene, M.; Knox, J. E.; Cross, J. B.; Bakken, V.; Adamo, C.; Jaramillo, J.; Gomperts, R.; Stratmann, R. E.; Yazyev, O.; Austin, A. J.; Cammi, R.; Pomelli, C.; Ochterski, J. W.; Martin, R. L.; Morokuma, K.; Zakrzewski, V. G.; Voth, G. A.; Salvador, P.; Dannenberg, J. J.; Dapprich, S.; Daniels, A. D.; Farkas, Ö.; Foresman, J. B.; Ortiz, J. V.; Cioslowski, J.; Fox, D. J. *Gaussian09*; Gaussian, Inc.: Wallingford, CT, 2009.

(23) Perdew, J. P.; Burke, K.; Ernzerhof, M. *Phys. Rev. Lett.* **1996**, *77*, 3865.

(24) Perdew, J. P.; Burke, K.; Ernzerhof, M. *Phys. Rev. Lett.* **1997**, *78*, 1396.

(25) Adamo, C.; Barone, V. *J. Chem. Phys.* **1999**, *110*, 6158.

(26) Hay, P. J.; Wadt, W. R. *J. Chem. Phys.* **1985**, *82*, 270.

(27) Hay, P. J.; Wadt, W. R. *J. Chem. Phys.* **1985**, *82*, 299.

(28) Gu, X.; Fei, T.; Zhang, H.; Xu, H.; Yang, B.; Ma, Y.; Liu, X. *J. Phys. Chem. A* **2008**, *112*, 8387.

(29) De Angelis, F.; Belpassi, L.; Fantacci, S. *J. Mol. Struct.* **2009**, *914*, 74.

(30) Bai, F.-Q.; Wang, J.; Xia, B.-H.; Pan, Q.-J.; Zhang, H.-X. *Dalton Trans* **2012**, *41*, 8441.

(31) Becke, A. D. *J. Chem. Phys.* **1993**, *98*, 5648.

(32) Lee, C.; Yang, W.; Parr, R. G. *Phys. Rev. B* **1988**, *37*, 785.

(33) Chipman, D. M. *J. Chem. Phys.* **2000**, *112*, 5558.

(34) Miertus, S.; Scrocco, E.; Tomasi, J. *Chem. Phys.* **1981**, *55*, 117.

(35) Segall, M. D.; Lindan, P. J. D.; Probert, M. J.; Pickard, C. J.; Hasnip, P. J.; Clark, S. J.; Payne, M. C. *J. Phys. Cond. Matter* **2002**, *14*, 2717.

(36) Webster, C.; Hall, M. B. *Coord. Chem. Rev.* **2003**, *238−239*, 315.

(37) Minaev, B.; Minaeva, V.; Agren, H. *J. Phys. Chem. A* **2009**, *113*, 726.

(38) Newman, P. D.; Cavell, K. J.; Hallett, A. J.; Kariuki, B. M. *Dalton Trans.* **2011**, *40*, 8807.

(39) Polson, M.; Ravaglia, M.; Fracasso, S.; Garavelli, M.; Scandola, F. *Inorg. Chem.* **2005**, *44*, 1282.

(40) Li, X.; Minaev, B.; Ågren, H.; Tian, H. *J. Phys. Chem. C* **2011**, *115*, 20724.

(41) Weng, Z. F.; Motherwell, W. D. S.; Allen, F. H.; Cole, J. M. *Acta Crystallogr. B* **2008**, *64*, 348.

(42) Weng, Z. F.; Motherwell, W. D. S.; Cole, J. M. *J. Appl. Crystallogr.* **2008**, *41*, 955.

(43) *Avogadro: An Open-Source Molecular Builder and Visualization Tool*, Version 1.0.3.

(44) Cole, J. M. *Analyst* **2012**, *136*, 448.

(45) Kovalevsky, A. Y.; Bagley, K. A.; Coppens, P. *J. Am. Chem. Soc.* **2002**, *124*, 9241.

(46) Kovalevsky, A. Y.; Bagley, K. A.; Cole, J. M.; Coppens, P. *Inorg. Chem.* **2003**, *42*, 140.

(47) Bowes, K. F.; Cole, J. M.; Husheer, S. L. G.; Raithby, P. R.; Savarese, T.; Sparkes, H. A.; Teat, S. J.; Warren, J. E. *Chem. Commun.* **2006**, 2448.

(48) Phillips, A. E.; Cole, J. M.; d'Almeida, T.; Low, K. S. *Inorg. Chem.* **2012**, *51*, 1204.

(49) Sylvester, S. O.; Cole, J. M.; Waddell, P. G. *J. Am. Chem. Soc.* **2012**, *134*, 11860.

(50) Chen, L. X.; Shaw, G. B.; Novozhilova, I.; Liu, T.; Jennings, G.; Attenkofer, K.; Meyer, G. J.; Coppens, P. *J. Am. Chem. Soc.* **2003**, *125*, 7022.

(51) Coppens, P.; Vorontsov, I. I.; Graber, T.; Kovalevsky, A. Y.; Chen, Y.-S.; Wu, G.; Gembicky, M.; Novozhilova, I. V. *J. Am. Chem. Soc.* **2004**, *126*, 5980.

(52) Ozawa, Y.; Pressprich, M. R.; Coppens, P. *J. Appl. Crystallogr.* **1998**, *31*, 128.

(53) Fullagar, W. K.; Wu, G.; Kim, C.; Ribaud, L.; Sagerman, G.; Coppens, P. *J. Synchrotron Rad.* **2000**, *7*, 229.

(54) Gembicky, M.; Oss, D.; Fuchs, R.; Coppens, P. *J. Synchrotron Rad.* **2005**, *12*, 665.

(55) Husheer, S. L. G.; Cole, J. M.; d'Almeida, T.; Teat, S. J. *Rev. Sci. Instrum.* **2010**, *81*, 043905.

(56) Phillips, A. E.; Cole, J. M.; d'Almeida, T.; Low, K. S. *Phys. Rev B* **2010**, *82*, 155118.

(57) Cole, J. M.; Waddell, P. G.; Jayatilaka, D. *Cryst. Growth Des.* **2012**, *12*, 2277.

(58) Chan, M. C. W.; Kui, S. C. F.; Cole, J. M.; McIntyre, G. J.; Matsui, S.; Zhu, N.; Tam, K.-H *Chem.—Eur. J.* **2006**, *12*, 2607.